

# 3D Instance Segmentation of MVS Buildings

Yanghui Xu, Jiazhou Chen\*, Shufang Lu, Ronghua Liang, and Liangliang Nan

**Abstract**—We present a novel framework for instance segmentation of 3D buildings from Multi-view Stereo (MVS) urban scenes. Unlike existing works focusing on semantic segmentation of an urban scene, the emphasis of this work lies in detecting and segmenting 3D building instances even if they are attached and embedded in a large and imprecise 3D surface model. Multi-view RGB images are first enhanced to RGBH images by adding a heightmap and are segmented to obtain all roof instances using a fine-tuned 2D instance segmentation neural network. Roof instance masks from different multi-view images are then clustered into global masks. Our mask clustering accounts for spatial occlusion and overlapping, which can eliminate segmentation ambiguities among multi-view images. Based on these global masks, 3D roof instances are segmented out by mask back-projections and extended to the entire building instances through a Markov random field (MRF) optimization. Quantitative evaluations and ablation studies have shown the effectiveness of all major steps of the method. A dataset for the evaluation of instance segmentation of 3D building models is provided as well. To the best of our knowledge, it is the first dataset for 3D urban buildings on the instance segmentation level<sup>1</sup>.

**Index Terms**—Instance segmentation, dataset, 3D urban scene, multi-view clustering.

## I. INTRODUCTION

In recent decades, the Multi-View Stereo (MVS) technique has been widely used in the GIS industry. Multi-view images are captured by Unmanned Aerial Vehicle (UAV) and used to automatically reconstruct dense 3D mesh models of large urban scenes [1], [2]. The reconstructed 3D mesh models provide a visually pleasing representation of urban scenes. However, due to the lack of semantic information, they can hardly be used directly in various real-world applications, such as urban planning, simulation, and solar potential estimation.

Buildings are the most important part of a city, its segmentation is the core of the semantic analysis of urban scenes. Rather than semantic segmentation, we focus on the instance segmentation of buildings, as it separates different building instances, even if they are attached. Thus, our goal is to segment all building instances in a large 3D urban scene precisely and automatically, as shown in Fig.1.

Recent advances in deep learning have achieved great success in image instance segmentation, but applying these techniques on 3D mesh models is still challenging and has not been sufficiently explored. Feature extraction of 3D data is the key to apply deep learning to the 3D model segmentation. Volumetric-based methods [3], [4], and point cloud-based

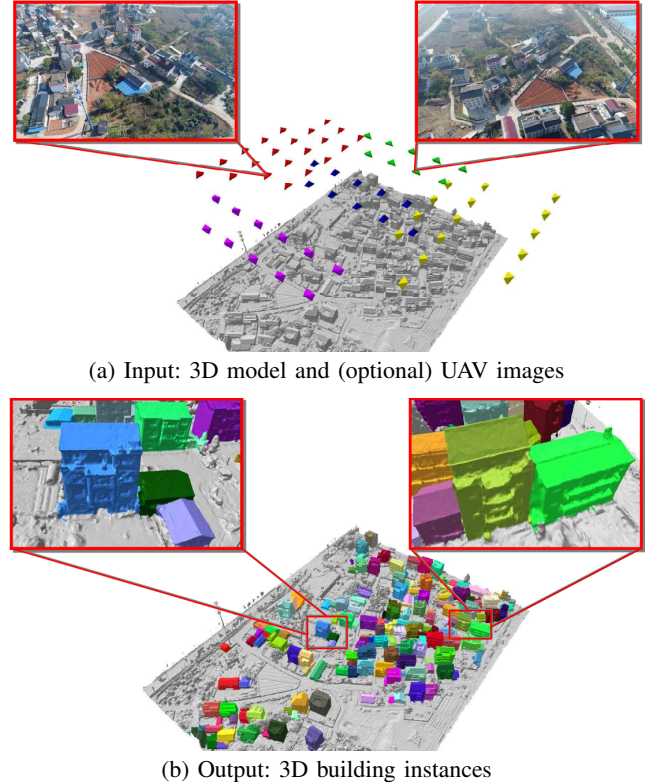


Fig. 1. Instance segmentation of 3D buildings in a large urban scene. The pyramids above the 3D scene model in (a) indicate the position and orientation of the cameras.

methods [5], [6] are limited by memory and computing power, thus are mainly used for the segmentation of relatively small indoor scenes [7], [8], [9], [10], [11], [12], which are not suitable for large-scale outdoor scenes. Besides, the lack of annotated 3D instance segmentation dataset for outdoor scenes also hinders the application of deep learning on instance segmentation of 3D urban scenes.

In this paper, we combine the MVS framework with a learning-based 2D instance segmentation method for buildings in large 3D urban scenes. Such a combination is not straightforward due to three main reasons.

First, instance segmentation on multi-view images creates a large number of instance masks while the masks corresponding to the same building are not associated with each other. Projecting the masks back to the 3D scene without correspondences will lead to instance ambiguities, as 2D instance masks from different views may be completely inconsistent, especially when the 3D mesh model has noises.

Second, the spatial distribution of buildings in urban scenes is quite diverse. Buildings in aerial images have various densities, shapes, and orientations. It is quite common in

\* Corresponding author

Y. Xu, J. Chen, S. Lu and R. Liang are with the School of Computer Science and Technology, Zhejiang University of Technology, China

L. Nan is with the Delft University of Technology, The Netherlands

<sup>1</sup>The datasets are available at xxxx [the link to the datasets will be inserted after the acceptance of the paper]

reality that some buildings (e.g., terraced houses) might be attached and cannot be visually separated even by human beings. Besides, other objects on the ground (e.g., greenhouses, gardens, and parking lots) may have building-like appearances, adding challenges to the instance segmentation.

Third, buildings in multi-view images are often partially occluded by attached ones or tall trees, in particular the lower parts of the facades. The spatial occlusion increases ambiguities in mask correspondences, which further makes instance segmentation of buildings more challenging.

To build mask correspondence among different multi-view images, we propose an instance mask clustering method. To improve segmentation accuracy for diversely distributed buildings, we enhance multi-view RGB images to RGBH images by adding an extra channel encoding the height information. To ease the spatial occlusion challenge, we perform instance segmentation of roofs instead of entire buildings, since roofs have higher visibility than other parts of buildings.

The core contributions of our work include:

- A multi-view instance segmentation framework that segments 3D buildings precisely in large urban scenes;
- An occlusion-aware clustering method for instance masks, which robustly eliminates ambiguities in mask correspondences among multi-view UAV images;
- A benchmark dataset *InstanceBuilding* for instance segmentation of 3D buildings in large urban scenes. The dataset consists of both roof instances in RGBH images and building instances in 3D mesh models.

## II. RELATED WORK

There is a large volume of research in instance segmentation for various data sources. In this section, we review the existing work of instance segmentation for both images and 3D data.

### A. Image instance segmentation

**Instance segmentation for natural images.** Existing instance segmentation methods for natural images can be classified into two categories: object detection-based approaches and metric learning-based ones. Object detection-based approaches work in a top-down manner and highly depend on object detection or proposal. R-CNN first introduces CNN in the field of object detection [13]. To improve computational efficiency, Fast R-CNN proposes an improved SPP (Spatial Pyramid Pooling) [14] structure named RoI pooling [15], and Faster R-CNN uses region proposal networks instead of selective searching to extract object candidates, which forms an efficient end-to-end network for object detection [16].

Based on Faster R-CNN [16], Mask R-CNN combines with FPN [17] to detect objects with different sizes and uses RoIAlign instead of RoI pooling to form a simple, flexible, and effective instance segmentation network [18]. Recently, mask scoring R-CNN uses mask scores to improve the category scores used in Mask R-CNN [19]. PANet uses a bottom-up annotation structure to shorten the information path and enhances the feature pyramid with accurate localization signals existing at low levels [20]. HTC combines detection and

segmentation with a multi-task and multi-stage hybrid cascade structure [21].

Many other dense instance segmentation methods are based on metric learning [22]. These methods work in a bottom-up manner, generate embedding features [23], [24] for each pixel and use post-processing methods such as clustering [25], [26] or graph theory [27] to classify these pixels. Inspired by FCIS [28] and YOLACT [29], BlendMask uses a blender module to merge top-level coarse instance information with lower-level fine granularities [30].

**Instance segmentation for aerial images.** In the last decade, instance segmentation methods for aerial images of urban scenes have also been proposed because of the wide applications of aerial images. Montoya et al. use an  $\alpha$ -shape algorithm to calculate the boundary polygons of building objects, which are further optimized by CRF [31]. By combining the CNN backbone with FPN and RNN, Li et al. propose an end-to-end deep neural network to predict polygon outlines of buildings and road topology maps [32]. Conv MPN uses GNN (graph neural network) [33] to reconstruct the building plan from a single image [34]. DARNet employs a polar representation of contours to predict contours that are free of self-intersection and a loss function consisting of a data term, a curvature term, and a balloon term, which not only encourages the predicted contours to match ground truth building boundaries but also prefers low-curvature solutions [35].

### B. 3D instance segmentation

Unlike images that inherently have a grid structure, the vertices and faces in discrete surfaces (i.e., 3D meshes) do not have regular spatial structures to be directly convoluted. Volumetric methods ease this issue using a 3D grid representation, which is notoriously expensive in terms of computational efficiency and memory consumption [4], [12], [36], [37], [38], [39].

Various strategies have been proposed to address the memory issue of volumetric methods. For example, OctNet uses an octree structure to avoid unnecessary cells [3], thus reducing memory consumption. PointNet uses T-net and max-pooling to achieve rotation invariance and the capability of handling unsorted 3D point clouds. It fuses both local and global features, making it an efficient and effective feature extractor for point cloud data [5]. Through point grouping and multi-level feature extraction, PointNet++ can better extract discriminative features for point clouds with uneven density [6].

Based on features extracted by PointNet, PointNet++, and PointCNN [40], many 3D instance segmentation methods for point clouds have also been proposed. SGPN predicts the instances by learning the similarity matrix between point clouds. However, the size of its similarity matrix tends to explode as the number of points increases [8]. GSPN extends the structure of Mask R-CNN (that was originally developed for images) to process 3D data [7]. JSNet [41] and ASIS [10] both learn the instance embedding space and combine semantic features and instance features of the point clouds to jointly improve the accuracy of semantic segmentation and instance segmentation.

Though great progress has been made for instance segmentation of indoor scenes. However, existing methods are

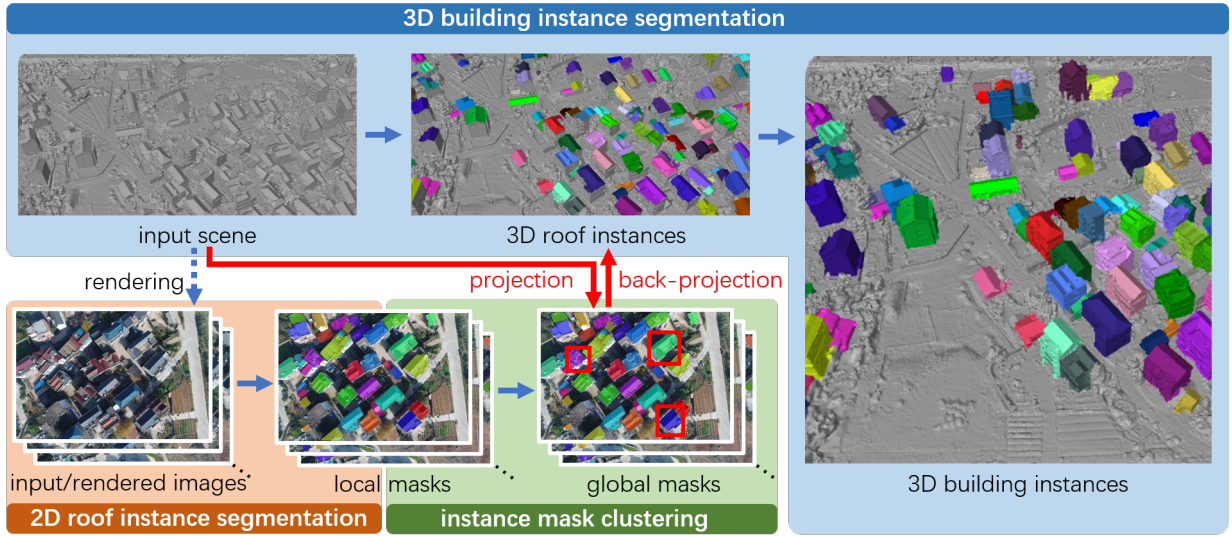


Fig. 2. An overview of the proposed method. Our method takes a 3D urban scene and optionally multi-view UAV images as input and segments all 3D building instances as results. It contains three major steps: 2D roof instance segmentation, instance mask clustering, and 3D building instance segmentation. The multi-view images are not obligatory, as they can also be generated by the rendering of the input 3D scene with textures (noted by the dotted arrow in the figure). The red rectangles highlight a few global masks selected by our clustering method. The projection and back-projection operations noted by the red arrows in the figure contribute to both instance mask clustering and the occlusion-aware 3D roof segmentation.

designed for processing point cloud data. It is still a challenge to extend these methods to outdoor scenes without sufficient annotated data and generalize them to handle the fast accumulation of urban models in the form of meshes. In this work, we establish a 3D instance segmentation dataset for urban scenes and propose the first framework for 3D instance segmentation of buildings from urban MVS meshes.

### III. METHODOLOGY

Compared to the lower parts of buildings that are more likely to be occluded by the nearby buildings and trees, building roofs usually have better visibility in aerial imaging. This observation motivates us to approach instance segmentation of entire buildings by looking into the segmentation of building roofs. In contrast to the previous work directly segmenting entire buildings [42], we perform roof segmentation by using a deep neural network. This strategy significantly improves the accuracy of the segmentation stage and simplifies the manual annotation in the data preparation stage.

One characteristic of our method is the hybrid process of 2D images and the corresponding 3D meshes, in which spatial occlusion is fully considered in processing the two distinctive data sources. Fig. 2 shows the proposed multi-view 3D instance segmentation framework that consists of three major steps:

- 1) **2D roof instance segmentation.** Roofs in multi-view images are automatically segmented by an instance segmentation neural network that is fine-tuned using our RGBH imagery dataset.
- 2) **Instance mask clustering.** An occlusion-aware clustering method for roof instance masks is exploited, which correlates instance masks from multi-view images to eliminate ambiguities. The mask clustering is the core of our method, which projects the 3D urban scene to

the image space to measure the spatial overlap between arbitrary pairs of instance masks.

- 3) **3D building instance segmentation.** The clustered masks are projected back to the 3D space to segment 3D roof instances and the entire buildings are segmented in the end through an MRF optimization.

In the following part of this section, we introduce these three major steps, the benchmark dataset, and the implementation details.

#### A. 2D Roof instance segmentation

The challenge in building instance segmentation lies in that the roofs of adjacent (or even attached) buildings may have very similar appearance despite the difference in the height of the buildings. In this work, we take advantage of the complementary characteristics of the images and the 3D model of the scene by enhancing each RGB aerial image to an RGBH image that provides additional geometric cues. Specifically, we render a heightmap for each drone image using the 3D urban models reconstructed from the drone images and camera parameters. We add an additional channel encoding the height information to the drone images to obtain RGBH images, in which the height values are separately normalized for each image. With the RGBH images, we apply Mask R-CNN [18] to segment roof instances automatically.

According to our quantitative evaluation on the benchmark dataset, the AP, AP50, and AP75 [43] of the segmentation of roof instances on RGBH images reaches 0.3588, 0.5349, and 0.4174 respectively, which are significantly higher compared to 0.3001, 0.4632, and 0.3512 achieved on RGB aerial images. This demonstrates the advantage of height information on the roof instance segmentation. A visual comparison is shown in Fig. 3. Ground objects like trees and vegetable field are



Fig. 3. Comparison of the segmentation results without and with height information. (a) An input test drone image. (b) The segmentation result using only the RGB image. The rectangles highlight three misclassified regions, i.e., a vegetable field (in red) and a wall (in green) of a building are segmented as roofs, and two roofs of attached buildings (in blue) are not separated. (c) The heightmap obtained by rendering the scene using the 3D model and the camera parameters. (d) The segmentation result using both the RGB image and the heightmap, where the vegetable field, wall, and roofs are all correctly separated.

successfully separated from buildings, even though some of them have visually indistinguishable textures with building roofs. The Mask R-CNN neural network also computes a probability for each instance mask to represent its prediction confidence. To avoid low-confident masks, we only use roof instance masks whose prediction confidence is higher than 70%.

### B. Instance mask clustering

After the roof instance segmentation, we obtain a set of roof instance masks from multi-view images, where multiple masks may correspond to the same roof. Since roofs of the same building in multiple views have been segmented independently, the correspondences between roof instance masks are not known. This results in that the number of instance masks is much larger than the number of roofs in the scene. To establish the correspondences between the masks from multi-view images, we refer to 3D roof instances by back-projecting the 2D roof masks onto the 3D model of the scene using the camera parameters. However, identifying masks that correspond to the same roof is challenging due to two main reasons: First, the 2D instance segmentation may have errors due to the limited capability of the neural network and the complex structure of the building roofs, as shown in the first row of Fig. 4. Second, the instance masks from different views are ambiguous due to different levels of spatial occlusion, as shown in the second row of Fig. 4.

To tackle these two challenges, we propose an instance mask clustering method that divides instance masks into different groups such that each group corresponds to a unique roof instance of an individual building. Representative masks are first selected from the segmented instance masks, and the remaining masks are merged to them according to mask similarity measures. For clarity, we refer to all roof instance masks in multi-view images as local masks, while the representative masks selected for clustering as global masks, as they represent unique building roofs across different images.

We first build a similarity matrix  $\mathcal{M}$  to measure the spatial overlap for each pair of local masks. Based on  $\mathcal{M}$ , a mask with confidence value  $\mathcal{C}$  to be selected as a global mask is computed for each local mask. Finally, all local masks are sorted in descending order to select reliable global masks and are clustered into groups according to their similarities with

the global masks. Note that each mask group contains only one global mask. We establish the mapping between all local masks and global masks. In the following, we elaborate on these steps in detail.

**Occlusion-aware mask similarity.** To measure the spatial overlap of two masks, we project 3D mesh triangles to the image using the camera parameters. We render a depth map with the GPU acceleration for each multi-view image and employ a depth test to check the visibility for all the vertices. For the  $i$ th local mask, we record a set of triangles  $S_i$  whose centers are projected within this local mask region. A similarity matrix  $\mathcal{M}_{n \times n}$  is then computed to quantify the spatial overlap between every pair of local masks, where  $n$  is the number of all local masks. The similarity element  $m_{ij}$  measures the intersection over union (i.e.,  $IoU$ ) between the  $i$ th and the  $j$ th local masks, i.e.,

$$m_{ij} = A(S_i \cap S_j) / A(S_i \cup S_j), \quad (1)$$

where  $A(S)$  is the surface area of the triangles in the set  $S$ .  $\mathcal{M}_{n \times n}$  is a symmetric matrix as  $m_{ij} = m_{ji}$ .

**Mask confidence.** Generally, an ideal global mask should have the most overlap with local masks that correspond to the same roof and have the least overlap with local masks that correspond to roofs of different buildings. To select such global masks, we estimate a confidence value  $\mathcal{C}$  for each local mask to evaluate the overall overlap with all other local masks in the scene. It is calculated as the sum of similarity elements on the  $i$ th row of the similarity matrix  $\mathcal{M}$ :

$$\mathcal{C}_i = \mathcal{P}_i \cdot \sum_{j=1}^n \mathcal{P}_j \cdot m_{ij}, \quad (2)$$

where  $\mathcal{P}_i$  is the probability value produced by the Mask R-CNN neural network,  $\mathcal{C}_i$  sums up the probability-weighted similarity elements of local masks. It makes sense because local masks with higher prediction confidences are more likely to be global masks.

However, there is still one drawback in Equation (2): local masks with large areas may suppress smaller ones because they likely overlap more with other local masks, and thus they obtain larger mask confidence values. It is apparent that local masks with larger areas are not always the ideal global masks. The top row of Fig.4 shows such a counter-example.

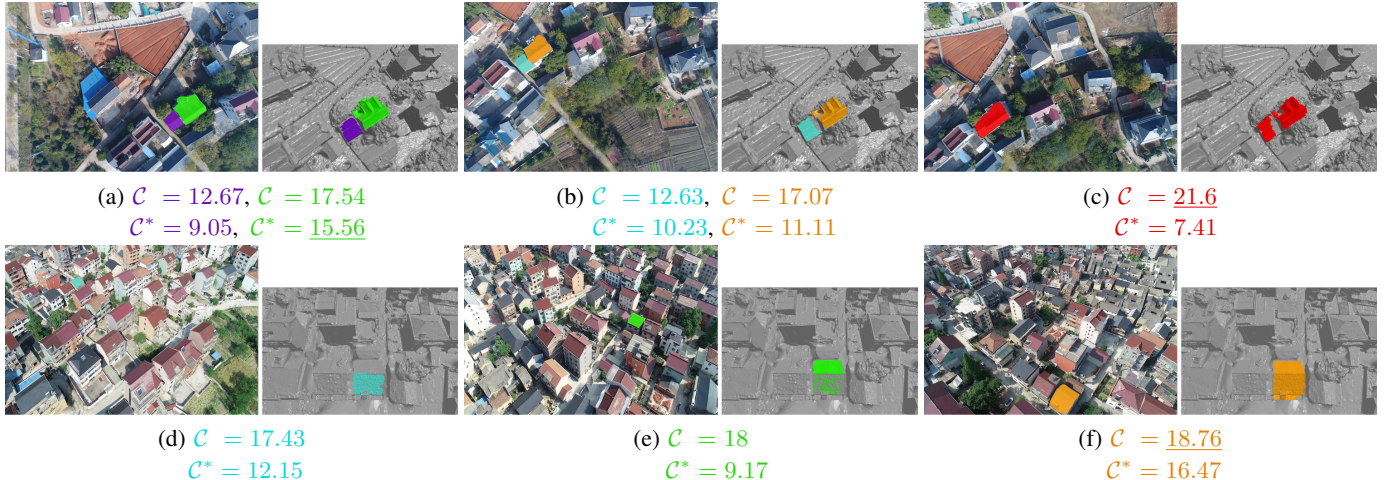


Fig. 4. Ambiguities in 2D roof instance segmentation. In each row, instance masks are shown in both the drone images (in different views) and the corresponding 3D mesh models (in an identical view). Top row: two roofs are separated in (a) and (b) but incorrectly mixed together in (c). Bottom row: (d) and (e) only cover a small part of the same roof, while (f) covers the entire roof. Original mask confidence values (denoted by  $\mathcal{C}$ ) and improved mask confidence values (denoted by  $\mathcal{C}^*$ ) are given in the sub-captions. The underlined numbers are the highest confidence values in each row.

To solve this issue, we define a binary term  $\Delta_{ij}$  to avoid such unexpected suppression:

$$\Delta_{ij} = \delta(m_{ij} - \beta), \quad (3)$$

where  $\delta(\cdot)$  is the delta function:

$$\delta(x) = \begin{cases} 0, & \text{if } x \leq 0 \\ 1, & \text{if } x > 0 \end{cases}. \quad (4)$$

With this binary term, the mask confidence is updated to:

$$\mathcal{C}_i^* = \mathcal{P}_i \cdot \sum_{j=1}^n \Delta_{ij} \cdot \mathcal{P}_j \cdot m_{ij}. \quad (5)$$

$\mathcal{C}_i^*$  sums up the similarity elements  $m_{ij}$  whose values are higher than a threshold  $\beta \in [0, 1]$  for each local mask. When  $\beta$  is close to 0,  $\Delta_{ij} = 1$  for most cases and thus  $\mathcal{C}_i^*$  degenerates to  $\mathcal{C}_i$ . When  $\beta$  is close to 1,  $\Delta_{ij}$  and  $\mathcal{C}_i^*$  are both close to 0, which means that the confidence values of all local masks to be selected as global masks are close to 0. In such a case, the clustering cannot distinguish global masks from local masks, resulting in false clustering in the end. In this work, we set  $\beta = 0.5$  in all our experiments, indicating that local masks with similarities (i.e., the ratio of the overlapping area) higher than  $\beta$  are considered in the computation of mask confidence values. More details about the evaluation of the parameter  $\beta$  can be found in the implementation details in Subsection IV-C.

**Mask clustering.** One key observation of this work is that local masks with higher confidence values are consistent with more other masks and thus should have higher priority to be selected as global masks, as shown in Fig. 4.

Based on the mask confidence, we employ a simple yet efficient order-based mask clustering. We first sort all local masks according to their confidence values  $\mathcal{C}^*$  and then traverse them in descending order to select global masks. In the traversing loop, if a local mask has not been marked, we mark it as a new global mask, and other non-marked local masks whose similarities with this global mask are higher

than  $\beta$  are considered consistent with this global mask, i.e.,  $\delta(m_{lg} - \beta) = 1$  where  $l$  and  $g$  are the indices of the local mask and this global mask, respectively. If a local mask has been already marked, we traverse to the next local mask until all of them are marked.

With the pre-computation of mask confidence values, the traversal is required only once. For efficiency, we establish a mapping table  $\mathbb{M}$  between all local masks to their corresponding global masks. It is worth noting that even we cannot guarantee each global mask in  $\mathbb{M}$  corresponds to a building instance in the real scene at this stage, a few false correspondences will not affect the final 3D instance segmentation. This will be explained in Subsection III-C.

### C. 3D building instance segmentation

**3D roof instance segmentation.** The existing multi-view semantic segmentation framework projects the 2D semantic labels back to the 3D model with the highest probability [44], [45]. For 3D instance segmentation, this framework is not suitable because the correspondences between local masks from multi-view images are unknown. Our mask clustering establishes the correspondences between the local masks from multiple views. We first project each vertex of the 3D model to all images and check its visibility using fields of view and depth maps. Then, using its corresponding local mask index at its projected position in the image, we retrieve its corresponding global mask from the mask mapping table  $\mathbb{M}$ .

For a vertex  $v$ , let  $MVI_v$  denote the set of multi-view images in which  $v$  is visible and  $GMI_p$  denote the global mask index corresponding to a multi-view image  $p$ . In some cases, a vertex  $v$  on the 3D surface model may be projected within multiple global masks. We denote the set of these global masks as  $\{GMI_p | p \in MVI_v\}$  and thus  $GMI_p = -1$  represents the background. From these global masks, the one with the largest quantity of corresponding local masks that were projected to by this vertex is associated with this vertex:

$$RID_v = \maxCount(\{GMI_p | p \in MVI_v\}), \quad (6)$$

where  $RID_v$  is the roof ID of vertex  $v$ , and the function  $\text{maxCount}(S)$  extracts the most occurring element in the set  $S$ . In case more than one global masks have the maximum count in the set  $S$ , the global mask with a smaller value of  $GMI$  will be chosen, as a smaller  $GMI$  value corresponds to a higher confidence of the global mask.

The advantage of determining the roof IDs in this way is that the most confident global mask can be automatically selected, and thus a user does not have to provide a specific number of target clusters (i.e., the number of global masks). This is because local masks with large errors in 2D roof segmentation are normally divided into groups containing small numbers of local masks. The global masks derived from these local masks usually have wrong predictions and therefore will be ignored in the upcoming 3D roof segmentation step, since only the global mask with the largest quantity of corresponding local masks is selected. Therefore, our 3D roof instance segmentation achieves higher prediction precision than the roof instance segmentation on the multi-view images. Their AP/AP50/AP75 values can be found in Subsection III-A and Table II respectively.

With the roof IDs for all vertices, the segmentation of the 3D model can be easily obtained. Specifically, the roof ID of a triangle face is determined by the majority of the vertices that indicate the same roof ID, i.e.,

$$RID_t = \text{maxCount}(\{RID_v | v \in V_t\}), \quad (7)$$

where  $RID_t$  represents the roof ID of triangle  $t$ , and  $V_t$  represents the three vertices of the triangle  $t$ .

**MRF-based 3D building segmentation.** Based on 3D roof segmentation, the next step is to segment the entire 3D buildings. We first estimate a Horizontal Oriented Bounding Box (*HOBB*) for each roof instance, as shown in Fig. 5. To segment an entire building from a 3D scene, we expand the *HOBB* on its four sides by a certain offset value (4 meters in all of our experiments). The triangles within the expanded *HOBB* (excluding those that have been labeled by other roof instances) are selected as a candidate building. We denote its triangle set as  $T = \{t_i\}$  and its edge set as  $E = \{e_{ij}\}$ , in which  $t_i$  represents the  $i$ th triangles in  $T$ , and  $e_{ij}$  represents the edge connecting  $t_i$  and  $t_j$ . We formulate the building segmentation as a foreground/background labeling process that minimizes the following energy function:

$$\psi(l) = \sum_{t_i \in T} \psi_{data}(l_i) + \sum_{e_{ij} \in E} \psi_{smooth}(l_i, l_j), \quad (8)$$

where  $l_i$  denotes the label of triangle  $t_i$  given by MRF-based segmentation.  $l_i = 1$  indicates the foreground (i.e., a building triangle) and  $l_i = 0$  the background (i.e., a non-building triangle).

The data term  $\psi_{data}(l_i)$  represents the penalty of assigning a label  $l_i$  to a triangle  $t_i$ . The 3D roof segmentation provides us a good foreground initialization, we denote its triangle set as  $T_f$ . We take triangles on the boundary of  $T$  as a background initialization, denoted as  $T_b$ . We further denote the set of other triangles in  $T$  as  $T_r$ . As shown in Fig. 7(a),  $T_f$ ,  $T_b$ , and  $T_r$  are visualized in red, green, and gray, respectively.

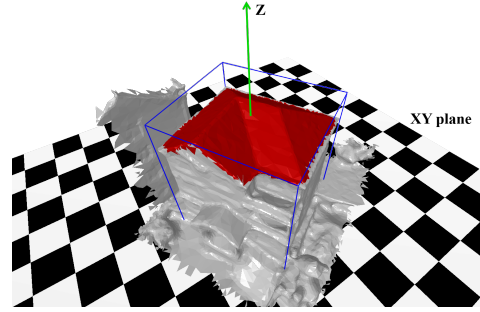


Fig. 5. Horizontal Oriented Bounding Box (*HOBB*). The top and bottom faces of the *HOBB* are horizontal, and the other four faces are oriented according to the PCA orientation estimation.

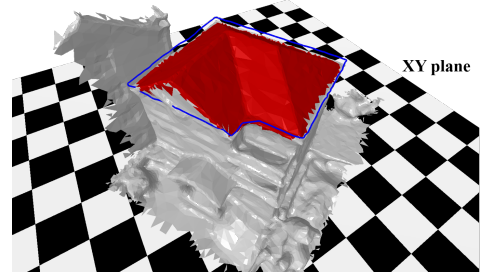


Fig. 6. Simplified roof boundary edge  $\mathcal{P}$ . The blue polygon represents the flat boundary of the roof on the XY plane. To make it easy to observe, we set its Z coordinate to be close to the height of the roof.

For triangles in  $T_r$ , our data term  $\psi_{data}(l_i)$  is defined as:

$$\psi_{data}(l_i) = \begin{cases} (1 + d_i) + \theta_i \cdot (1 + d_i) & \text{if } l_i = 1 \\ 1 & \text{if } l_i = 0 \end{cases}. \quad (9)$$

Before explaining the meaning of  $d_i$  and  $\theta_i$ , we define  $\mathcal{P}$ , a 2D polygon representing the simplified roof boundary edges, as shown in Fig. 6. We first extract boundary edges of the roof triangles using the Alpha Shape algorithm [46]. Then, we reduce the dimension of these boundary edges to the 2D horizontal plane by discarding their height and further simplify them through a RANSAC process [47]. The RANSAC process iteratively merges outline points of roofs to their neighbors if they are approximately collinear. The process stops until no more points can be merged. The simplified roof boundary edges constitute a 2D polygon that is referred to as the roof profile, denoted as  $\mathcal{P}$ . For each triangle  $t_i \in T_r$ , we find a line segment in  $\mathcal{P}$  with a minimal distance to the center of  $t_i$ . We denote this minimal distance as  $d_i$ , and the cosine of the horizontal angle between the normal of  $t_i$  and the direction of this line segment as  $\theta_i$ .  $\theta_i = 0$  when the normal of  $t_i$  is perpendicular to this line segment, and  $\theta_i = 1$  when their horizontal angle is 0. Then  $d_i$  is normalized by the maximum distance in the *HOBB*, and we sign the distance as negative if  $t_i$  is inside of  $\mathcal{P}$ . To make the foreground penalty and background penalty comparable on the roof profile (i.e., both penalties equal to 1 when  $d_i = 0$  and  $\theta_i = 0$ ), we use  $1 + d_i$  instead of  $d_i$ .

In Equation 9, the  $(1 + d_i)$  term is a distance constraint that guarantees only triangles close to  $\mathcal{P}$  are taken into the

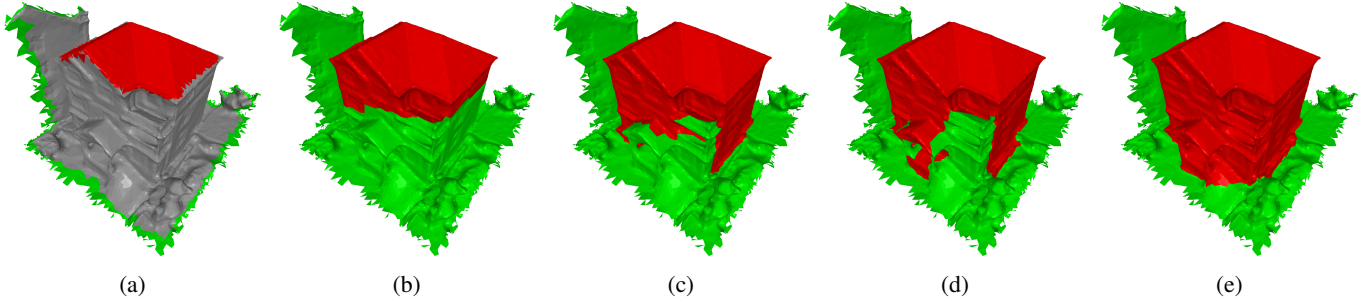


Fig. 7. 3D building segmentation based on MRF optimization. (a) Initial segmentation by the projection of 2D roof onto the 3D model (foreground in red and background in green). (b) Result of direct MRF optimization, where the initial roof segmentation misses the balcony and the gate shelter. (c) Our segmentation result without the orientation constraint. (d) Our segmentation result without the distance constraints. (e) Our segmentation result with both orientation and distance constraints.

building. The  $\theta_i \cdot (1 + d_i)$  term is an orientation constraint that guarantees that only triangles having similar orientations with the closest line segment are taken. The  $(1 + d_i)$  multiplication is to reduce the orientation constraint if the triangles are far away from  $\mathcal{P}$ .

The smoothness term  $\psi_{smooth}(l_i, l_j)$  penalizes adjacent triangles  $t_i$  and  $t_j$  being assigned with different labels. We take the cosine angle between normals of adjacent triangles as the penalty for assigning different labels to the adjacent triangle pair, i.e.,

$$\psi_{smooth}(l_i, l_j) = \begin{cases} \|n_i \cdot n_j\| & \text{if } l_i \neq l_j \\ 0 & \text{if } l_i = l_j \end{cases}. \quad (10)$$

Using the angles between faces,  $\psi_{smooth}(l_i, l_j)$  favors segmentation at sharp edges rather than at planar regions.

#### D. Benchmark dataset

We have created a benchmark dataset *InstanceBuilding* to evaluate our 3D instance segmentation method. We annotated 3D roofs and entire buildings for 4 large 3D urban scenes. Table I shows detailed information about these scenes, and their visualization can be found in Fig. 8 and the supplementary video. Note that about 2/3 buildings are attached to others and the town is quite crowded, as shown in the last column of Table I. Multi-view images in the first two scenes are captured by UAVs, while the multi-view images in the last two scenes are rendered using 3D urban scenes from a set of different viewpoints sampled randomly at 70 meters higher than the average height of these scenes separately. At each viewpoint, 5 virtual cameras facing down, front, back, left, and right are placed. The 3D urban scenes were reconstructed using *Bentley Acute3D ContextCapture*<sup>2</sup> from multi-view images.

We have developed a simple brush-based interactive tool to annotate all 3D roofs and building instances for each urban scene. Similar to most 2D annotation tools [48] which automatically extract the pixels of an object by marking the closed boundary polygon of the object. Our tool allows a user to casually draw strokes on the building boundaries and then the entire building can be automatically extracted.

For the training of 2D Roof instance segmentation, 608 random images were selected from around 20 thousand drone

TABLE I  
STATISTICS ON THE 3D MODELS OF OUR *InstanceBuilding* DATASET.

Scene	#Vertices	#Triangles	Area (km <sup>2</sup> )	#Images (resolution)	#Buildings
#1	1.13M	2.26M	0.076	79 (5472×3648)	185 / 145
#2	0.87M	1.72M	0.097	64 (5472×3078)	119 / 40
#3	1.14M	2.28M	0.081	284 (1916×994)	322 / 232
#4	0.60M	1.20M	0.18	240 (1536×994)	266 / 185

images. These images are acquired in more than 10 different cities by a consumer DJI drone Phantom 4 Pro with different cameras and flight altitudes. The images have different resolutions and have 27.3 buildings on average. All roofs in the selected images were manually annotated to train an instance segmentation neural network. 10 architecture students were invited to annotate all roofs in the 608 drone images. These 608 images are divided into 2 groups, 524 images for training and 84 images for testing.

For accuracy and efficiency consideration, we modified the LabelMe [48] toolkit to visualize the corresponding heightmap window alongside the drone image window. By synchronizing the annotation on both the image window and the heightmap window, volunteers can freely annotate on either of them. Based on our time recording of volunteer annotation, this double-window strategy saves the volunteers more than half of the time.

Our dataset *InstanceBuilding* contains both instance segmentation of roofs from images and building instance segmentation from 3D scenes. Compared to existing datasets, such as MSCOCO [43], Cityscapes [49], and PASCALVOC [50], our dataset focuses on roof instance segmentation in high-resolution images and building instance segmentation from 3D models. Compared to other remote sensing imagery datasets, such as SpaceNet [51] and xView [52], our dataset has higher resolution and richer angles of pitch. With the increasing popularity of low-altitude UAV capturing devices, we believe that our dataset will play an important role in applications such as urban planning, smart cities, and other related fields.

#### E. Implementation details

**2D roof segmentation.** We use the TensorFlow implementation of Mask R-CNN released by Matterport [53] for roof

<sup>2</sup><https://www.bentley.com/en/products/brands/contextcapture>

instance segmentation from images. The manually labeled images (see Subsection III-D) were used to fine-tune the Mask R-CNN network trained previously using the COCO dataset [43].

**MRF-based segmentation.** With the aforementioned MRF setting, we treat Equation 8 as a classical max-flow/min-cut optimization and solve it using the graph cut algorithm [54]. The MRF-based segmentation result is shown in Fig. 7 (e). To prove the validity of Equation 9, we simply set the penalties to 1 for both foreground and background in Equation 9, as the triangles in  $T_r$  have no explicit foreground/background priorities. As a result, it does not produce correct segmentation as expected, as shown in Fig. 7 (b). Comparisons in Fig. 7 (c) and (d) show that the introduction of the orientation and the distance constraint overcomes the interference of structural variations and noises in the MRF optimization, thus improving the 3D building segmentation.

#### IV. RESULTS AND DISCUSSION

We have evaluated our method with both drone images and virtually rendered images. All experiments were carried out on a machine with an Intel Core i7 processor, 32 GB memory, and an NVidia GeForce 1080 GPU.

##### A. Qualitative results

We tested our method on four scenes (see Fig. 8), for which the statistics are shown in Table I. Scene #1 and Scene #2 have UAV images and the corresponding camera parameters, while Scene #3 and Scene #4 do not have UAV images. Thus for Scene #3 and Scene #4, we rendered images from multiple viewpoints and performed instance segmentation. The roof instance segmentation results are shown in Fig. 8 (middle column) and the 3D building instance segmentation results are shown in Fig. 8 (right column). We can see that our approach successfully segmented most buildings, even if they are dense, varying in style, and attached to each other.

##### B. Ablation Study

We have evaluated our results on the 3D mesh models in the *InstanceBuilding* benchmark dataset. We first computed the *IoUs* between predictions and the ground truth based on the area of the mesh triangles. Then we used the commonly used instance-level evaluation metrics, namely AP, AP50, and AP75, in all evaluations [43], where AP50/AP75 indicates the average precision when *IoU* threshold is set to 0.5/0.75, and AP is averaged over 10 *IoU* thresholds of 0.5:0.05:0.95.

**Height information.** As have already been demonstrated in Fig. 3, using RGBH images significantly improves the 2D roof instance segmentation. To understand how the height information improves 3D roof instance segmentation and its effects on 3D building instance segmentation, we have conducted a comparison on the four large 3D scenes from *InstanceBuilding* both with and without height information, using two different clustering methods, i.e., the spectral clustering and our method. The results of the comparison are given in Table II and Table III. These comparisons have revealed that our method using

RGBH images achieves higher accuracy than the one without height information (i.e., using RGB images). This is because that the additional heightmaps provide spatial information of the urban scenes to the neural network model, which makes the roofs and buildings more distinguishable.

**The multi-view framework.** The 2D segmentation in our method is applied to multi-view images, rather than orthophoto maps. To understand the advantages of this multi-view framework, we have also implemented an orthophoto-based instance segmentation solution for comparison. We first generated the orthophoto maps and their corresponding heightmaps of the same scenes through a render-to-texture technique. These two types of maps were combined to form the orthophoto RGBH maps, which were then used to detect the 2D roof instances. Since there was almost no occlusion for the roofs in the orthophoto maps, mask clustering was not necessary and we directly applied the 3D building segmentation to produce the final results. The statistics of the results are reported in Table IV.

From this comparison, we can see that our multi-view based method achieves higher AP than the orthophoto-based method. Our investigation showed that the 2D roof instance segmentation for multi-view drone images and orthophoto maps have similar accuracy. The key advantage of our multi-view based method lies in mask clustering that integrates multiple segmentation results of the identical roofs from different viewpoints, which can be regarded as a cross-correction process. Our multi-view based method not only eliminates most of the incorrect instance masks from individual multi-view images but also recovers a more complete set of instances by complementing the information from different views. Besides, we also found that our method can better segment attached building instances than the orthophoto-based method.

**Mask clustering.** The instance mask clustering is crucial to overcome the ambiguities in the multi-view instance masks. Many clustering methods are available in the literature, such as Mean-shift [55] and K-means [56], but none of them is suitable for our multi-view scenario. This is mainly because it is still unknown how to design comparable features for masks from different views, especially when they have a large variation in the viewpoints. Compared to viewpoint-variant features, the spatial overlap between masks can be calculated accurately. Therefore, we directly calculate a similarity matrix using the spatial overlap between masks, rather than their features.

Moreover, clustering methods like Mean-shift and K-means require computing the mean of some features, which makes them not suitable for our task without a good feature extractor. For example, the position, size, mean color of masks cannot accurately describe their features. The other difficulty of these clustering methods is to choose the optimal values of parameters, such as the kernel function for Mean-shift, and the K value for K-means. Note that our clustering method does not require specifying the number of target clusters, which is the core advantage of our method.

Based on the similarity matrix, one alternative option for mask clustering is spectral clustering [57]. We have evaluated it with different numbers of target clusters, noted as  $K$ , and compared our clustering method with spectral clustering. For

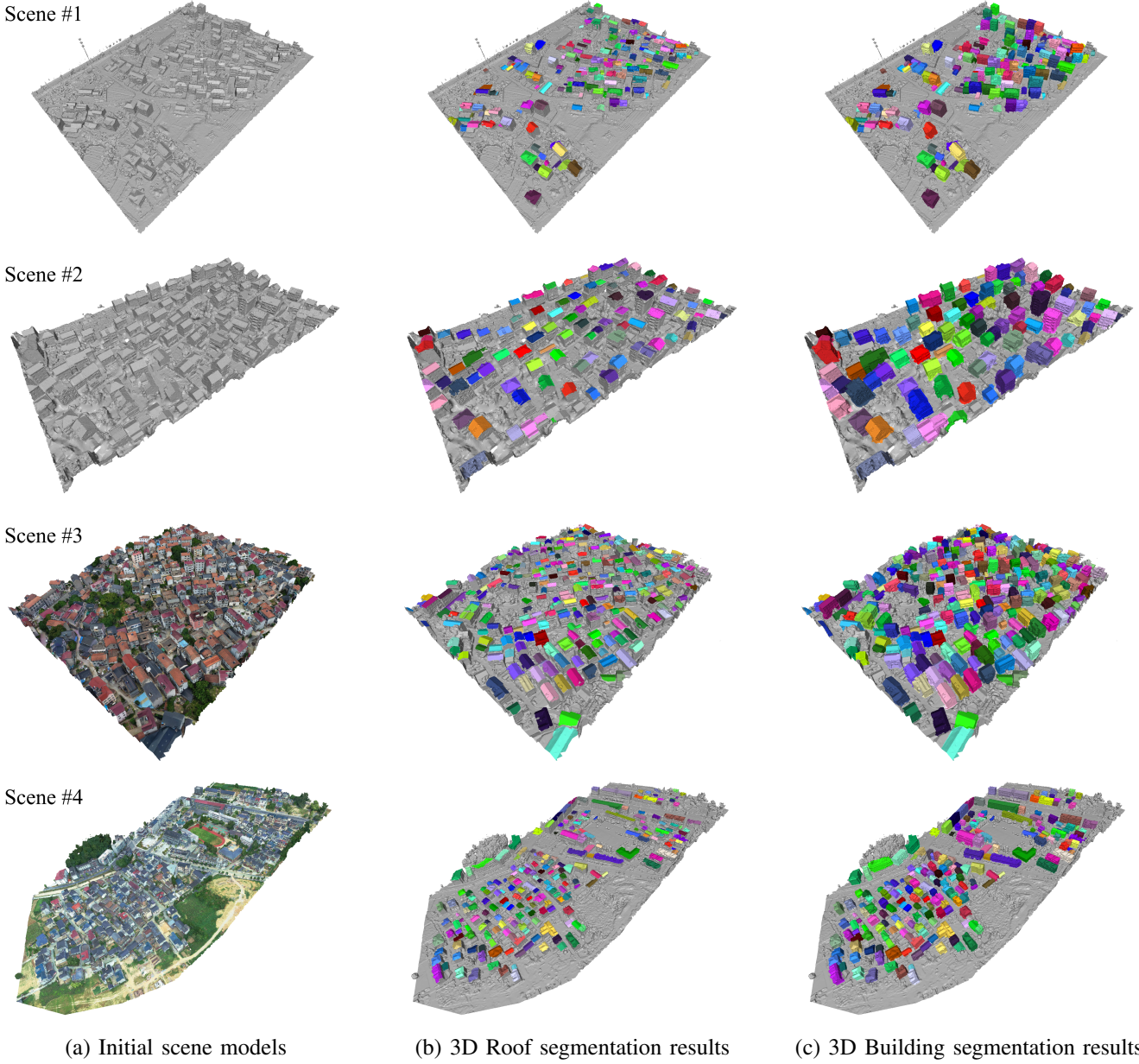


Fig. 8. Building instance segmentation results of four scenes. The two scenes on the top have UAV images and their camera parameters, while the scenes #3 and #4 in the bottom do not have UAV images, for which we render images from multiple viewpoints instead.

TABLE II  
COMPARISON OF FOUR DIFFERENT CLUSTERING METHODS ON 3D *roof* INSTANCE SEGMENTATION.

Scene	Spectral with RGB ( $K_1$ )			Spectral with RGBH ( $K_1$ )			Spectral with RGB ( $K_2$ )			Spectral with RGBH ( $K_2$ )			Ours with RGB			Ours with RGBH		
	AP	AP50	AP75	AP	AP50	AP75	AP	AP50	AP75	AP	AP50	AP75	AP	AP50	AP75	AP	AP50	AP75
#1	0.5836	0.7784	0.6420	0.6810	0.8264	0.7097	0.5705	0.8011	0.6250	0.6619	0.8636	0.7159	0.6142	0.8182	0.6818	<b>0.7267</b>	<b>0.9034</b>	<b>0.8011</b>
#2	0.4388	0.5950	0.4545	0.4702	0.6116	0.4628	0.4521	0.6198	0.4876	0.4689	0.6471	0.4874	0.5231	0.6860	0.5620	<b>0.6091</b>	<b>0.7438</b>	<b>0.6446</b>
#3	0.5586	0.7107	0.5982	0.5793	0.7278	0.6391	0.4118	0.5905	0.4722	0.4651	0.6036	0.5089	0.6059	0.7574	0.6568	<b>0.6195</b>	<b>0.8142</b>	<b>0.7225</b>
#4	0.3259	0.6090	0.3008	0.4414	0.7180	0.4361	0.4162	0.7143	0.3910	0.4222	0.7406	0.4098	0.4519	0.7594	0.4023	<b>0.4703</b>	<b>0.7744</b>	<b>0.4586</b>

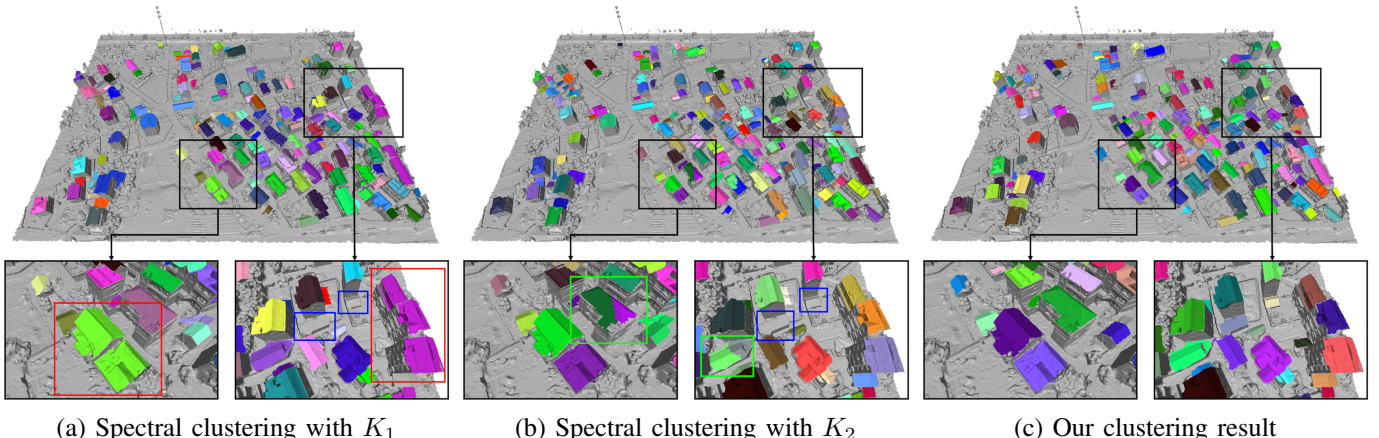


Fig. 9. Comparison of roof mask clustering of three methods on Scene #1. (a) Spectral clustering using the ground truth number of targets  $K_1$  tends to under-segment (red rectangles) and miss (blue rectangles) some buildings. (b) Spectral clustering using the number of global masks  $K_2$  estimated by our method tends to over-segment (green rectangles) and miss (blue rectangles) some buildings. (c) Our clustering method achieves more precise roof instance segmentation without specifying the target number.

TABLE III  
COMPARISON OF FOUR DIFFERENT CLUSTERING METHODS ON 3D BUILDING INSTANCE SEGMENTATION.

Scene	Spectral with RGB ( $K_1$ )			Spectral with RGBH ( $K_1$ )			Spectral with RGB ( $K_2$ )			Spectral with RGBH ( $K_2$ )			Ours with RGB			Ours with RGBH		
	AP	AP50	AP75	AP	AP50	AP75	AP	AP50	AP75	AP	AP50	AP75	AP	AP50	AP75	AP	AP50	AP75
#1	0.6059	0.7730	0.6324	0.6827	0.8341	0.7276	0.6211	0.8216	0.6216	0.6903	0.8432	0.7351	0.6519	0.8216	0.6811	<b>0.7270</b>	<b>0.8595</b>	<b>0.7730</b>
#2	0.4437	0.6218	0.4538	0.4899	0.6387	0.4874	0.4689	0.6471	0.4874	0.5328	0.6891	0.5462	0.5571	0.7143	0.5714	<b>0.6202</b>	<b>0.7227</b>	<b>0.6471</b>
#3	0.5332	0.7640	0.5839	0.5602	0.7671	0.6149	0.4519	0.6447	0.5122	0.4904	0.6615	0.5248	0.6208	0.8261	0.6739	<b>0.6270</b>	<b>0.8354</b>	<b>0.7019</b>
#4	0.4467	0.6391	0.4323	0.5677	0.7218	0.5902	0.5523	0.7556	0.5564	0.5767	0.7782	0.5977	0.5906	<b>0.7970</b>	0.5977	<b>0.6117</b>	0.7895	<b>0.6353</b>

a fair comparison, we used two different values of  $K$  for the spectral clustering method on each scene: 1)  $K_1$ : the building number from the statistics on the 3D evaluation dataset, and 2)  $K_2$ : the number of global masks estimated by our clustering method. Note that  $K_2$  is typically larger than  $K_1$ , as some of the global masks did not correspond to real 3D buildings. A more detailed explanation is given in Subsection III-C. Specifically,  $K_1$  has a value of 185/185, 119/119, 322/322, 266/266, and  $K_2$  has a value of 386/431, 204/318, 730/704, 595/615 for Scene #1, #2, #3, and #4 with RGB/RGBH images, respectively.

The advantage of our clustering method over spectral clustering can also be concluded from Table II and Table III. No matter on 3D roof or building instance segmentation, using  $K_1$  or  $K_2$ , with or without height information, our clustering method always reaches higher precision than spectral clustering. Besides, the last term (“Ours with RGBH”) of Table II also shows that we achieve higher AP/AP50/AP75 on the 3D roof instance segmentation than on the aerial images (values are shown in Subsection III-A), because our occlusion-aware mask clustering suppresses false prediction from individual images and thus improves the overall segmentation precision.

A visual comparison with our clustering method and the spectral clustering for Scene #1 is shown in Fig. 9. From this comparison, we can observe that spectral clustering misses some roofs and is also confused by roofs of attached buildings when  $K = K_1$ . Besides, it over-segments and misses roofs when  $K = K_2$ . In contrast, our instance mask clustering successfully segments roof instances precisely without specifying the number of target roofs. More visual comparison results

TABLE IV  
COMPARISON BETWEEN OUR FRAMEWORK BASED ON MULTI-VIEW IMAGES AND THE ONE BASED ON ORTHOPHOTO MAPS.

Scene	Orthophoto-based			Ours (multi-view)		
	AP	AP50	AP75	AP	AP50	AP75
#1	0.6751	<b>0.8595</b>	0.7189	<b>0.7270</b>	<b>0.8595</b>	<b>0.7730</b>
#2	0.5969	0.7176	0.5847	<b>0.6202</b>	<b>0.7227</b>	<b>0.6471</b>
#3	0.5475	0.8199	0.5714	<b>0.6270</b>	<b>0.8354</b>	<b>0.7019</b>
#4	0.6079	<b>0.7895</b>	0.6278	<b>0.6117</b>	<b>0.7895</b>	<b>0.6353</b>

can be found in the supplementary video.

**MRF-based building segmentation.** As shown in Fig. 7, the orientation and distance constraints are important to achieve accurate 3D building segmentation. We have also evaluated the segmentation precision and recall by omitting one of them. The results are reported in Table V, from which we can conclude that the distance constraint plays a more important role than the orientation constraint, but the best segmentation accuracy can only be achieved if they are both employed.

### C. Effects of parameters

Our method involves a few parameters, among which  $\beta$  in the mask clustering step is the only parameter that we leave tunable for users (while all other parameters are fixed). In this subsection, we discuss how this parameter affects mask clustering.

Intuitively, the meaning of  $\beta$  parameter in our work is very similar to the threshold parameter of  $IoU$  in many existing

TABLE V  
COMPARISON OF USING DIFFERENT SEGMENTATION CONSTRAINTS ON 3D *building* INSTANCE SEGMENTATION.

Scene	Without the orientation constraint			Without the distance constraint			With both constraints		
	AP	AP50	AP75	AP	AP50	AP75	AP	AP50	AP75
#1	0.6286	0.8432	0.6811	0.6600	0.8449	0.7297	<b>0.7270</b>	<b>0.8595</b>	<b>0.7730</b>
#2	0.3908	0.6891	0.3529	0.5193	<b>0.7311</b>	0.6387	<b>0.6202</b>	0.7227	<b>0.6471</b>
#3	0.3537	0.7391	0.2919	0.4472	0.8261	0.4472	<b>0.6270</b>	<b>0.8354</b>	<b>0.7019</b>
#4	0.4707	0.7556	0.4737	0.5620	0.7870	0.6241	<b>0.6117</b>	<b>0.7895</b>	<b>0.6353</b>

object detection works where a mask is considered to be correctly predicted when the *IoU* between the detection mask and the ground truth is greater than this threshold. Empirically, this threshold is initially set to 0.5. Similarly, in our mask clustering, if the *IoU* of the two local masks is greater than  $\beta$ , they should be considered to belong to the same group. That is, they represent the same roof instance. In this work, we initially set  $\beta = 0.5$  in all of our experiments. To determine the optimal value for  $\beta$ , we experimented with different values on all 4 scenes. As we can see from Fig. 10, the AP, AP50, and AP75 are always close to the highest values when  $\beta = 0.5$ . Note that slightly increasing/reducing  $\beta$  reduces/increases the confidence values but barely affects the ordering of the masks. This reveals that our mask clustering is tolerant to the  $\beta$  parameter.

#### D. Running time

The training took around 3 hours with 8 loops. The overall running time on segmenting a scene varied from 6 to 8 minutes, depending on the scene size, image resolution, and the number of images. The MRF optimization took around 2.5 minutes on average for each scene. The graphics rendering for multi-view image generation (only for scenes without drone images), 3D vertex projection for the overlapping computation, and heightmap generation were accelerated using the GPU, which took less than 1 minute. The mask clustering took only 1 second, which was much faster than many other traditional clustering methods.

#### E. Discussions

**Applications.** We have implemented a simple building simplification prototype using a RANSAC-based plane fitting [47] and plane regularization. Based on our 3D building instance segmentation, 3D buildings in large urban scenes are automatically simplified, as shown in Fig. 11. In such an application, instance segmentation is obligatory, as semantic segmentation is insufficient to separate individual buildings. We believe our 3D building instance segmentation method can benefit more smart city applications, such as urban planning.

**Limitations.** Since our approach falls into the multi-view paradigm, it heavily relies on the quality of the 2D instance segmentation. Roof types that do not exist in the training dataset may not be precisely segmented. Two such examples are shown in Fig. 12. In Fig. 12 (a), a gate shelter was not reliably detected in the 2D roof segmentation step, and in Fig. 12 (b), a tall tree was segmented as a part of the nearby building. Enriching the training dataset may partially solve this

issue. In addition, developing a neural network dedicated to separating roofs and trees may produce more reliable instance segmentation results.

## V. CONCLUSION AND FUTURE WORK

We have presented a multi-view framework for instance segmentation of 3D urban buildings. Based on occlusion-aware similarity matrices, a novel instance mask clustering method is proposed to eliminate the mask ambiguities among multi-view images. To further improve segmentation accuracy, roofs (instead of buildings) are firstly segmented, and RGB images are enriched with heightmaps. Our method takes full advantage of the multi-view framework to precisely segment 3D buildings in large urban scenes.

We have collected and annotated an RGBH drone imagery dataset and a 3D building instance segmentation dataset, named *InstanceBuilding*. We believe the new dataset could benefit research in 3D instance segmentation for various urban applications. Since most of the state-of-the-art learning-based 3D instance segmentation methods focus on indoor scenes, our multi-view instance segmentation framework explores a new avenue for large outdoor scenes.

**Future work.** Our work focuses on buildings because they are the most important ingredients in the urban environment. This research comes from a real-world project addressing urban management issues. However, our multi-view 3D instance segmentation framework is general and can be extended to other urban objects and even indoor scenes. To do this, the neural network and MRF-based optimization have to be adapted, which are trivial but out of the scope of our focus. Applying the system on point clouds of urban scenes is also an interesting and challenging problem, we leave this as our future work.

## REFERENCES

- [1] H.-H. Vu, P. Labatut, J.-P. Pons, and R. Keriven, “High accuracy and visibility-consistent dense multiview stereo,” *IEEE transactions on pattern analysis and machine intelligence*, vol. 34, no. 5, pp. 889–901, 2012.
- [2] Y. Yao, Z. Luo, S. Li, T. Fang, and L. Quan, “Mvsnet: Depth inference for unstructured multi-view stereo,” *arXiv preprint arXiv:1804.02505*, 2018.
- [3] G. Riegler, A. Osman Ulusoy, and A. Geiger, “Octnet: Learning deep 3d representations at high resolutions,” in *Proceedings of the IEEE Conference on Computer Vision and Pattern Recognition*, 2017, pp. 3577–3586.
- [4] D. Maturana and S. Scherer, “Voxnet: A 3d convolutional neural network for real-time object recognition,” in *2015 IEEE/RSJ International Conference on Intelligent Robots and Systems (IROS)*. IEEE, 2015, pp. 922–928.

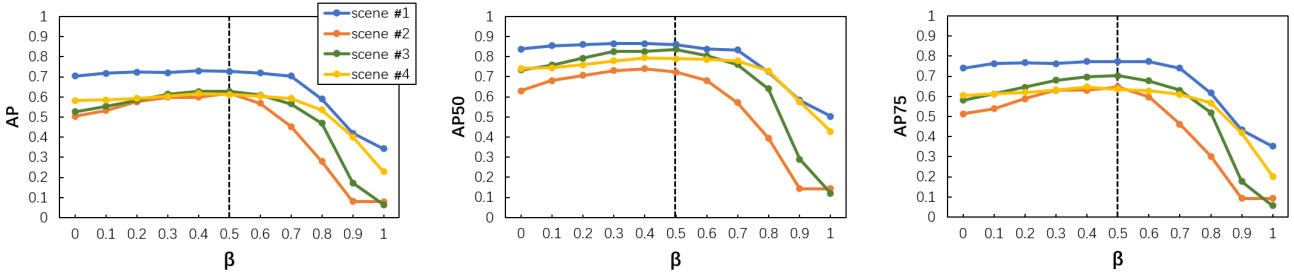


Fig. 10. Evaluation of the segmentation results with different  $\beta$  values. The AP (left), AP50 (middle), and AP75 (right) of the segmentation result are always close to the highest values when  $\beta = 0.5$ .

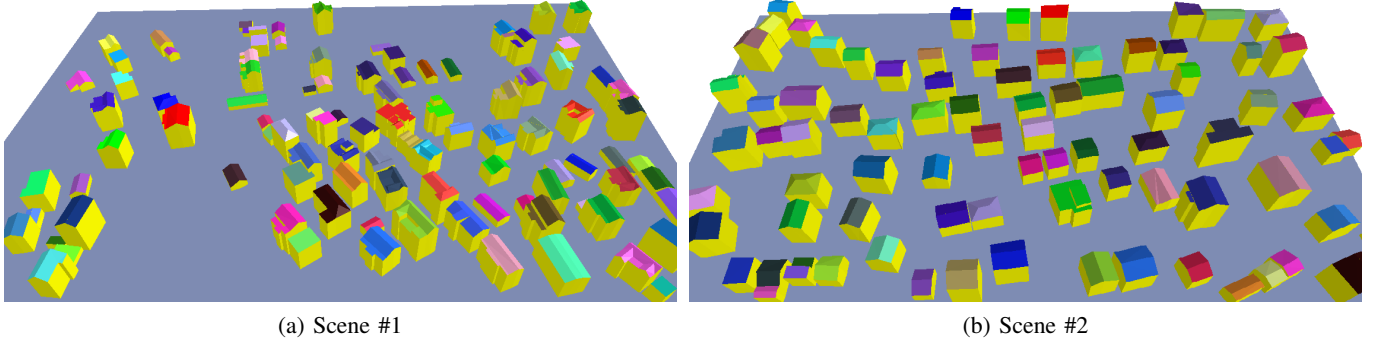


Fig. 11. Automatic simplification of buildings in two large urban scenes. The results are obtained by applying RANSAC for plane extraction followed by plane regularization.

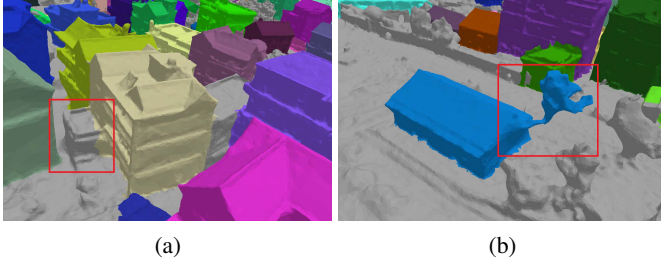


Fig. 12. Two failure cases of our method. (a) A gate shelter was not segmented as part of the roof in the image segmentation stage. (b) A tall tree was segmented as a roof instance because it has a similar height and texture as its nearby building.

[5] C. R. Qi, H. Su, K. Mo, and L. J. Guibas, “Pointnet: Deep learning on point sets for 3d classification and segmentation,” in *Proceedings of the IEEE conference on computer vision and pattern recognition*, 2017, pp. 652–660.

[6] C. R. Qi, L. Yi, H. Su, and L. J. Guibas, “Pointnet++: Deep hierarchical feature learning on point sets in a metric space,” in *Advances in neural information processing systems*, 2017, pp. 5099–5108.

[7] L. Yi, W. Zhao, H. Wang, M. Sung, and L. J. Guibas, “Gspn: Generative shape proposal networks for 3d instance segmentation in point cloud,” in *Proceedings of the IEEE conference on computer vision and pattern recognition*, 2019, pp. 3947–3956.

[8] W. Wang, R. Yu, Q. Huang, and U. Neumann, “Sgpn: Similarity group proposal network for 3d point cloud instance segmentation,” in *Proceedings of the IEEE Conference on Computer Vision and Pattern Recognition*, 2018, pp. 2569–2578.

[9] J. Hou, A. Dai, and M. Nießner, “3d-sis: 3d semantic instance segmentation of rgb-d scans,” in *Proceedings of the IEEE Conference on Computer Vision and Pattern Recognition*, 2019, pp. 4421–4430.

[10] X. Wang, S. Liu, X. Shen, C. Shen, and J. Jia, “Associatively segmenting instances and semantics in point clouds,” in *Proceedings of the IEEE Conference on Computer Vision and Pattern Recognition*, 2019, pp. 4096–4105.

[11] Q.-H. Pham, T. Nguyen, B.-S. Hua, G. Roig, and S.-K. Yeung, “Jsis3d: Joint semantic-instance segmentation of 3d point clouds with multi-task pointwise networks and multi-value conditional random fields,” in *Proceedings of the IEEE/CVF Conference on Computer Vision and Pattern Recognition*, 2019, pp. 8827–8836.

[12] C. Liu and Y. Furukawa, “Masc: multi-scale affinity with sparse convolution for 3d instance segmentation,” *arXiv preprint arXiv:1902.04478*, 2019.

[13] R. Girshick, J. Donahue, T. Darrell, and J. Malik, “Rich feature hierarchies for accurate object detection and semantic segmentation,” in *Proceedings of the IEEE conference on computer vision and pattern recognition*, 2014, pp. 580–587.

[14] K. He, X. Zhang, S. Ren, and J. Sun, “Spatial pyramid pooling in deep convolutional networks for visual recognition,” *IEEE transactions on pattern analysis and machine intelligence*, vol. 37, no. 9, pp. 1904–1916, 2015.

[15] R. Girshick, “Fast r-cnn,” in *Proceedings of the IEEE international conference on computer vision*, 2015, pp. 1440–1448.

[16] S. Ren, K. He, R. Girshick, and J. Sun, “Faster r-cnn: Towards real-time object detection with region proposal networks,” in *Advances in neural information processing systems*, 2015, pp. 91–99.

[17] T.-Y. Lin, P. Dollár, R. Girshick, K. He, B. Hariharan, and S. Belongie, “Feature pyramid networks for object detection,” in *Proceedings of the IEEE conference on computer vision and pattern recognition*, 2017, pp. 2117–2125.

[18] K. He, G. Gkioxari, P. Dollár, and R. Girshick, “Mask r-cnn,” in *Proceedings of the IEEE international conference on computer vision*, 2017, pp. 2961–2969.

[19] Z. Huang, L. Huang, Y. Gong, C. Huang, and X. Wang, “Mask scoring r-cnn,” in *Proceedings of the IEEE conference on computer vision and pattern recognition*, 2019, pp. 6409–6418.

[20] S. Liu, L. Qi, H. Qin, J. Shi, and J. Jia, “Path aggregation network for instance segmentation,” in *Proceedings of the IEEE conference on computer vision and pattern recognition*, 2018, pp. 8759–8768.

[21] K. Chen, J. Pang, J. Wang, Y. Xiong, X. Li, S. Sun, W. Feng, Z. Liu, J. Shi, W. Ouyang *et al.*, “Hybrid task cascade for instance segmentation,” in *Proceedings of the IEEE conference on computer vision and pattern recognition*, 2019, pp. 4974–4983.

[22] B. De Brabandere, D. Neven, and L. Van Gool, “Semantic instance segmentation with a discriminative loss function,” *arXiv preprint arXiv:1708.02551*, 2017.

[23] A. Fathi, Z. Wojna, V. Rathod, P. Wang, H. O. Song, S. Guadarrama,

and K. P. Murphy, "Semantic instance segmentation via deep metric learning," *arXiv preprint arXiv:1703.10277*, 2017.

[24] D. Novotny, S. Albanie, D. Larlus, and A. Vedaldi, "Semi-convolutional operators for instance segmentation," in *Proceedings of the European Conference on Computer Vision (ECCV)*, 2018, pp. 86–102.

[25] X. Liang, L. Lin, Y. Wei, X. Shen, J. Yang, and S. Yan, "Proposal-free network for instance-level object segmentation," *IEEE transactions on pattern analysis and machine intelligence*, vol. 40, no. 12, pp. 2978–2991, 2017.

[26] S. Kong and C. C. Fowlkes, "Recurrent pixel embedding for instance grouping," in *Proceedings of the IEEE Conference on Computer Vision and Pattern Recognition*, 2018, pp. 9018–9028.

[27] M. Bai and R. Urtasun, "Deep watershed transform for instance segmentation," in *Proceedings of the IEEE Conference on Computer Vision and Pattern Recognition*, 2017, pp. 5221–5229.

[28] Y. Li, H. Qi, J. Dai, X. Ji, and Y. Wei, "Fully convolutional instance-aware semantic segmentation," in *Proceedings of the IEEE Conference on Computer Vision and Pattern Recognition*, 2017, pp. 2359–2367.

[29] D. Bolya, C. Zhou, F. Xiao, and Y. J. Lee, "Yolact: Real-time instance segmentation," in *Proceedings of the IEEE international conference on computer vision*, 2019, pp. 9157–9166.

[30] H. Chen, K. Sun, Z. Tian, C. Shen, Y. Huang, and Y. Yan, "Blendmask: Top-down meets bottom-up for instance segmentation," in *Proceedings of the IEEE/CVF Conference on Computer Vision and Pattern Recognition*, 2020, pp. 8573–8581.

[31] J. A. Montoya-Zegarra, J. D. Wegner, K. Schindler *et al.*, "Semantic segmentation of aerial images in urban areas with class-specific higher-order cliques," *ISPRS Annals of the Photogrammetry, Remote Sensing and Spatial Information Sciences*, vol. 2, pp. 127–133, 2015.

[32] Z. Li, J. D. Wegner, and A. Lucchi, "Topological map extraction from overhead images," in *Proceedings of the IEEE International Conference on Computer Vision*, 2019, pp. 1715–1724.

[33] P. W. Battaglia, J. B. Hamrick, V. Bapst, A. Sanchez-Gonzalez, V. Zam baldi, M. Malinowski, A. Tacchetti, D. Raposo, A. Santoro, R. Faulkner *et al.*, "Relational inductive biases, deep learning, and graph networks," *arXiv preprint arXiv:1806.01261*, 2018.

[34] F. Zhang, N. Nauata, and Y. Furukawa, "Conv-mpn: Convolutional message passing neural network for structured outdoor architecture reconstruction," in *Proceedings of the IEEE/CVF Conference on Computer Vision and Pattern Recognition*, 2020, pp. 2798–2807.

[35] D. Cheng, R. Liao, S. Fidler, and R. Urtasun, "Darnet: Deep active ray network for building segmentation," in *Proceedings of the IEEE Conference on Computer Vision and Pattern Recognition*, 2019, pp. 7431–7439.

[36] A. Dai, D. Ritchie, M. Bokeloh, S. Reed, J. Sturm, and M. Nießner, "Scanscomplete: Large-scale scene completion and semantic segmentation for 3d scans," in *Proceedings of the IEEE Conference on Computer Vision and Pattern Recognition*, 2018, pp. 4578–4587.

[37] Z. Wu, S. Song, A. Khosla, F. Yu, L. Zhang, X. Tang, and J. Xiao, "3d shapenets: A deep representation for volumetric shapes," in *Proceedings of the IEEE conference on computer vision and pattern recognition*, 2015, pp. 1912–1920.

[38] P.-S. Wang, Y. Liu, Y.-X. Guo, C.-Y. Sun, and X. Tong, "O-cnn: Octree-based convolutional neural networks for 3d shape analysis," *ACM Transactions on Graphics (TOG)*, vol. 36, no. 4, pp. 1–11, 2017.

[39] A. Dai, C. Ruizhongtai Qi, and M. Nießner, "Shape completion using 3d-encoder-predictor cnns and shape synthesis," in *Proceedings of the IEEE Conference on Computer Vision and Pattern Recognition*, 2017, pp. 5868–5877.

[40] Y. Li, R. Bu, M. Sun, W. Wu, X. Di, and B. Chen, "Pointcnn: Convolution on x-transformed points," in *Advances in neural information processing systems*, 2018, pp. 820–830.

[41] L. Zhao and W. Tao, "Jsnnet: Joint instance and semantic segmentation of 3d point clouds," in *AAAI*, 2020, pp. 12 951–12 958.

[42] M. Li, L. Nan, N. Smith, and P. Wonka, "Reconstructing building mass models from uav images," *Computers & Graphics*, vol. 54, pp. 84–93, 2016.

[43] T.-Y. Lin, M. Maire, S. Belongie, J. Hays, P. Perona, D. Ramanan, P. Dollár, and C. L. Zitnick, "Microsoft coco: Common objects in context," in *European conference on computer vision*. Springer, 2014, pp. 740–755.

[44] A. Kundu, Y. Li, F. Dellaert, F. Li, and J. M. Rehg, "Joint semantic segmentation and 3d reconstruction from monocular video," in *ECCV*. Springer International Publishing, 2014, pp. 703–718.

[45] M. Bláha, C. Vogel, A. Richard, J. D. Wegner, T. Pock, and K. Schindler, "Large-scale semantic 3d reconstruction: An adaptive multi-resolution model for multi-class volumetric labeling," in *2016 IEEE Conference on Computer Vision and Pattern Recognition (CVPR)*, June 2016, pp. 3176–3184.

[46] F. Bernardini and C. L. Bajaj, "Sampling and reconstructing manifolds using alpha-shapes," in *In Proc. 9th Canad. Conf. Comput. Geom*, 1997, p. pages.

[47] R. Schnabel, R. Wahl, and R. Klein, "Efficient ransac for point-cloud shape detection," *Computer Graphics Forum*, vol. 26, no. 2, pp. 214–226, 2007.

[48] B. C. Russell, A. Torralba, K. P. Murphy, and W. T. Freeman, "Labelme: A database and web-based tool for image annotation," *International Journal of Computer Vision*, vol. 77, no. 1, pp. 157–173, May 2008. [Online]. Available: <https://doi.org/10.1007/s11263-007-0090-8>

[49] M. Cordts, M. Omran, S. Ramos, T. Rehfeld, M. Enzweiler, R. Benenson, U. Franke, S. Roth, and B. Schiele, "The cityscapes dataset for semantic urban scene understanding," in *Proceedings of the IEEE conference on computer vision and pattern recognition*, 2016, pp. 3213–3223.

[50] M. Everingham, L. Van Gool, C. K. Williams, J. Winn, and A. Zisserman, "The pascal visual object classes (voc) challenge," *International journal of computer vision*, vol. 88, no. 2, pp. 303–338, 2010.

[51] A. Van Etten, D. Lindenbaum, and T. M. Bacastow, "Spacenet: A remote sensing dataset and challenge series," *arXiv preprint arXiv:1807.01232*, 2018.

[52] D. Lam, R. Kuzma, K. McGee, S. Dooley, M. Laielli, M. Klaric, Y. Bulatov, and B. McCord, "xview: Objects in context in overhead imagery," *arXiv preprint arXiv:1802.07856*, 2018.

[53] W. Abdulla, "Mask r-cnn for object detection and instance segmentation on keras and tensorflow," 2017.

[54] Y. Y. Boykov and M. . Jolly, "Interactive graph cuts for optimal boundary region segmentation of objects in n-d images," in *Proceedings Eighth IEEE International Conference on Computer Vision. ICCV 2001*, vol. 1, July 2001, pp. 105–112 vol.1.

[55] D. Comaniciu and P. Meer, "Mean shift: A robust approach toward feature space analysis," *IEEE Transactions on pattern analysis and machine intelligence*, vol. 24, no. 5, pp. 603–619, 2002.

[56] T. Kanungo, D. M. Mount, N. S. Netanyahu, C. D. Piatko, R. Silverman, and A. Y. Wu, "An efficient k-means clustering algorithm: Analysis and implementation," *IEEE transactions on pattern analysis and machine intelligence*, no. 7, pp. 881–892, 2002.

[57] U. Von Luxburg, "A tutorial on spectral clustering," *Statistics and computing*, vol. 17, no. 4, pp. 395–416, 2007.